Transcriptional Diversity of Medium Spiny Neurons in the Primate Striatum

Authors: Jing He[1], Michael Kleyman[2], Jianjiao Chen[1], Aydin Alikaya[1], Kathryn M. Rothenhoefer[1], Bilge Esin Ozturk[3], Morgan Wirthlin[2], Kenneth Fish[4], Leah C.T. Byrne[3]*, Andreas R. Pfenning[2]*, William R. Stauffer[1]*.

Affiliations:

[1]Department of Neurobiology, Systems Neuroscience Center, Brain Institute, Center for Neuroscience, Center for the Neural Basis of Cognition, University of Pittsburgh.

[2]Department of Computational Biology, School of Computer Science, Neuroscience Institute, Center for the Neural Basis of Cognition, Carnegie Mellon University.

[3]Department of Ophthalmology, Brain Institute, Center for Neuroscience, Center for the Neural Basis of Cognition, University of Pittsburgh.

[4]Department of Psychiatry, University of Pittsburgh.

*Correspondence to: wrs@pitt.edu (W.R.S.), apfenning@cmu.edu (A.R.P.), lbyrne@pitt.edu (L.C.T.B.)

Abstract

The striatum is the neural interface between dopamine reward signals and cortico-basal ganglia circuits responsible for value assignments, decisions, and actions. Medium spiny neurons (MSNs) make up the vast majority of striatal neurons and are traditionally classified as two distinct types: direct- and indirect-pathway MSNs. The direct- and indirect-pathway model has been useful for understanding some aspects of striatal functions, but it accounts for neither the anatomical heterogeneity, nor the functional diversity of the striatum. Here, we use single nucleus RNA-sequencing and Fluorescent In-Situ Hybridization to explore MSN diversity in the Rhesus macaque striatum. We identified MSN subtypes that correspond to the major subdivisions of the striatum. These include dorsal striatum subtypes associated with striosome and matrix compartments, as well as ventral striatum subtypes associated with the shell of the nucleus accumbens. We also describe a cell type that is anatomically restricted to "Neurochemically Unique Domains in the Accumbens and Putamen (NUDAPs)". Together, these results help to advance nonhuman primate studies into the genomics era. The identified cell types provide a comprehensive blueprint for investigating cell type-specific information processing, and the differentially expressed genes lay a foundation for achieving cell type-specific transgenesis in the primate striatum.

Main Text:

The striatum serves as the major input nucleus for the basal ganglia and the principal neural interface between dopamine reward signals and cortico-basal ganglia-thalamic circuits. Medium Spiny Neurons (MSNs), also known as Spiny Projection Neurons (SPNs), account for the vast majority of all striatal neurons (DiFiglia et al., 1976). D1-MSNs express dopamine receptor type 1 (*DRD1*) and their monosynaptic projections to the basal ganglia output nuclei form the "direct pathway." D2-MSNs express dopamine receptor type 2 (*DRD2*) and form the "indirect pathway," via di-synaptic projections to the basal ganglia output nuclei (Parent and Hazrati, 1995). Broadly, activity in the direct and indirect pathways produces opposing effects on thalamocortical projections. This cell type-specific circuit model has been crucial to understanding the role of the basal ganglia in the control of movement and the mechanisms of Parkinson's disease (Albin et al., 1989; DeLong and Wichmann, 2015), but it does not account for the anatomical and functional variation between the distinct neurochemical compartments in the dorsal striatum, nor does it explain the neurochemical heterogeneity or functional diversity of the ventral striatum.

In the dorsal striatum, direct and indirect pathway information processing occurs within segregated neurochemical compartments known as striosome and matrix (Graybiel and Ragsdale, 1978). Functionally, these compartments are thought to reflect their respective inputs and participate in limbic and sensorimotor functions (Gerfen, 1984; Graybiel and Ragsdale, 1978; Hong et al., 2019). The ventral striatum includes the nucleus accumbens (NAc), olfactory tubercle, and interface islands (Daunais et al., 2001; Haber and McFarland, 1999; Heimer and Wilson, 1975; Voorn et al., 1996). Moreover, the NAc itself is divided into core and shell territories that contribute differentially to reward processing, action selection, and decision making (Floresco, 2015). Together, these anatomically segregated striatal regions suggest that there is greater MSN heterogeneity than is predicted by D1- and D2- MSNs. To address these discrepancies, recent studies have employed single cell technologies that classify cell types

61 according to their gene expression (Tang et al., 2009). Single cell studies have revealed new
62 types of MSNs and striatal interneurons (Gokce et al., 2016; Krienen et al., 2020; Martin et al.,
63 2019; Muñoz-Manchado et al., 2018; Saunders et al., 2018; Stanley et al., 2019). Moreover,
64 single cell studies are providing novel insights into cell type-specific mechanisms for diseases
65 involving the striatum, including drug addiction (Savell et al., 2020) and Huntington's disease
66 (Lee et al., 2020). Despite these advances, we know neither the extent of MSN diversity in the
67 primate striatum, nor how that diversity corresponds to the anatomical or neurochemical
68 divisions of the highly articulated primate brain.

69 NHP brains and behaviors are more human-like than those of any other animal species
70 in which invasive neurophysiological experiments are possible. Thus, NHP studies are
71 indispensable for understanding the cell types, circuits, and systems that coordinate
72 sophisticated behaviors and malfunction during debilitating neurological, neurodegenerative,
73 and psychiatric diseases. Here, we set out to identify MSN subtypes in Rhesus macaque
74 monkeys. We used single nucleus RNA-sequencing (snRNA-Seq) and Fluorescent In-Situ
75 Hybridization (FISH) to characterize the transcriptional and anatomical diversity of MSNs and
76 closely related neurons. Our results indicate that the MSN subtypes, each of which was
77 distinguished by subtype-specific differentially expressed genes, reflect the major anatomical
78 and neurochemical divisions, including striosome and matrix compartments of the dorsal
79 striatum, the core and shell regions of the NAc, and the ventral interface islands including the
80 Islands of Calleja (ICj) and Neurochemically Unique Domains in the Accumbens and Putamen
81 (NUDAPs) (Voorn et al., 1996). The cell type-specific gene expression within these subtypes
82 provide insights into their functions and indicate potential molecular access points for cell type-
83 specific applications of genetically coded tools to primate brains in scientific or translational
84 settings.

85

86 **Results**

Major cell classes in primate striatum

To investigate the cell type-specific transcriptional architecture of the NHP striatum, we isolated the caudate (Cd), putamen (Pt), and ventral striatum (VS) from coronal sections of two monkeys and prepared single nuclei suspensions (Fig. 1a, Methods). We performed droplet-based RNA capture and sequenced the resulting barcoded cDNA libraries (Methods). To optimally align and count the transcripts, we re-annotated the Rhesus macaque reference genome (rheMac10) using a 'lift-over' of the human transcriptome

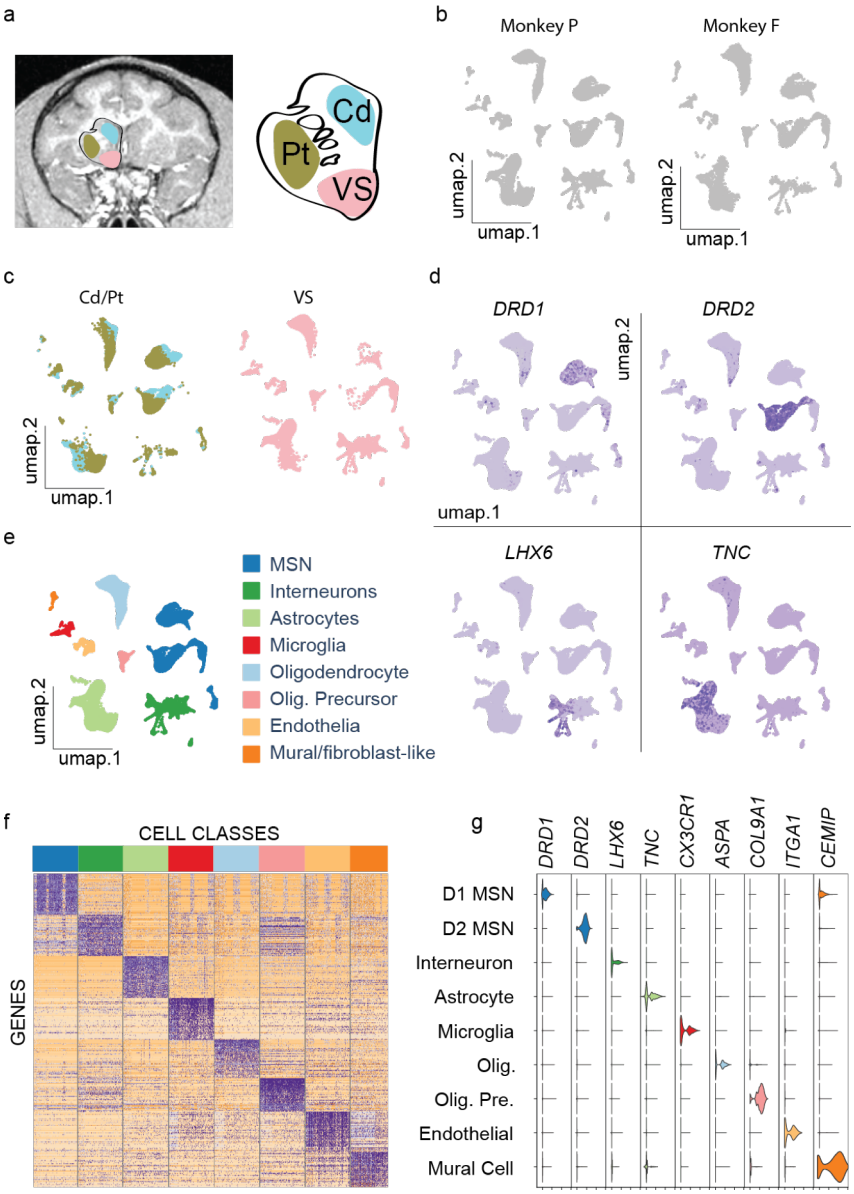

Figure 1. Cell type taxonomy in striatum. (a) MRI image of a Rhesus macaque coronal brain section (left) showing three striatal regions labeled by three patches (blue, caudate; green, putamen; pink, ventral striatum). Schematic striatum (right) marked by Cd (caudate), Pt (putamen), and VS (Ventral Striatum). **(b)** UMAP visualizations of the samples from the two subjects. **(c)** UMAP visualizations of striatal nuclei colored by the three regions. **(d)** Feature plots of canonical neuronal and astrocyte marker gene expression in striatal nuclei. **(e)** UMAP visualization colored according to eight major classes in the NHP. **(f)** Heat map of differentially expressed genes. Color bar at the top corresponds to the major classes identified in **e**. **(g)** Violin plots of distributions of marker gene expression across nine clusters, with MSNs being divided into D1- and D2-MSNs.

annotation (see Methods); a process that improves comparisons across species (Zhu et al., 2014). The custom annotation increased the reads confidently mapped to the genome by more than 10% (Fig. S1). We used Seurat to integrate the datasets from both monkeys (Methods). Side by side comparison of the nuclei from both subjects confirmed successful integration (Fig. 1b). After removing artifacts, we recovered the gene expression profiles from approximately 70,000 nuclei in two monkeys (F and P). These profiles were used for all subsequent analysis.

To identify the major cell classes in the striatum, we clustered the nuclei based on their gene expression counts (see Methods). Side-by-side comparison of nuclei from the two monkeys demonstrated broad similarities between the samples (Fig. 1b). Each major cluster had nuclei derived from the caudate, putamen, and ventral striatum, indicating broad similarities between the cell type compositions of each region (Fig. 1c). We made feature plots of well-known marker genes, including *DRD1* and *DRD2* for D1- and D2-MSNs, *LHX6* for interneurons, and *TNC* for astrocytes (Fig. 1d). Similarly, we identified oligodendrocytes, oligodendrocyte precursors, microglia, and other non-neuronal cell types (Fig. S2). Each major cell class was signified by groups of differentially expressed genes that were specifically enriched in that cluster (Fig. 1e,f and Table S1). We compared the intersection of differentially expressed genes from each cluster with marker gene lists from several databases (Gokce et al., 2016; Saunders et al., 2018; Zhang et al., 2014). This comparison confirmed the identity of the clusters and that they corresponded to the major cell classes in the striatum ($P < 0.05$, Benjamini-Hochberg corrected, Hypergeometric test). Violin plots showing the expression levels of marker genes in each major class including *DRD1* and *DRD2* for different types of MSNs confirmed the basic validity of our experimental and analytic methods (Fig. 1g). Together, these results provide a broad transcriptional catalog of cell classes in the NHP striatum.

Transcriptional diversity of Medium Spiny Neurons

According to our primary interest in MSN diversity, we sought to isolate and analyze MSN nuclei. We identified all neurons according to the expression of *RBFOX3*, the gene that codes for the neuron-specific marker NeuN (Fig. S3a). The *RBFOX3*-positive population included interneurons and MSNs. Interneurons were signified by their expression of *LHX6* (Fig. 1d), whereas MSNs were signified by well-known MSN-specific genes, including *PP1R1B*, *BCL11B*, and *PDE1B* (Fig. S3b-d) (Arlotta et al., 2008; Xie et al., 2006). We used these MSN markers to isolate MSN nuclei. Differential gene analysis of the isolated MSNs versus all other cell types revealed several other MSN markers, including *KIAA1211L*,

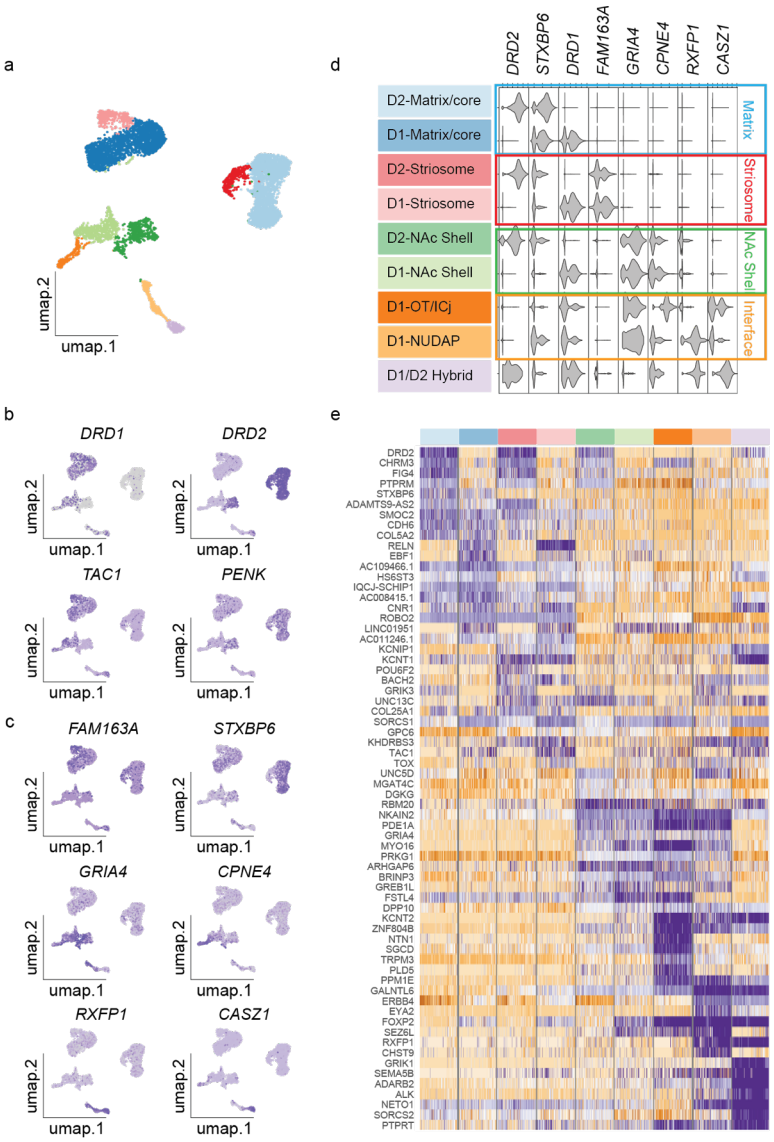

Figure 2. MSN transcriptional diversity. **(a)** UMAP projection of MSN nuclei. Each dot represents a nucleus and the colors represent the different MSN subtypes. **(b)** Feature plots for the expression of *DRD1*, *TAC1*, *DRD2*, *PENK* show the separation of D1- and D2-MSNs. **(c)** Feature plots showing marker genes most enriched in each cluster. **(d)** (left) MSN subtype identifications colored according to **a**. (right) Violin plots showing cell type and compartment specific marker gene expression. **(e)** Heatmap showing the top ten most enriched genes in each MSN subtype. Colored bar at the top corresponds to the colors in **a**.

163 *PDE2A, SLIT3*, and *NGEF* (Fig. S3e-h).

164 We clustered the MSNs at a resolution that best reflected the functional divisions in the
165 striatum, including direct and indirect pathways, striosome and matrix compartments, and core
166 and shell territories (methods). This resulted in nine clusters (Fig. 2a). Feature plots of canonical
167 D1- and D2-MSN markers showed that the clusters maintained clear separation between
168 *DRD1*- and *DRD2*-expressing nuclei (Fig. 2b). To identify and annotate the clusters, we used
169 previously described marker genes for striatal regions (Crittenden and Graybiel, 2011; Märtin et
170 al., 2019; Smith et al., 2016), the distributions of nuclei derived from dorsal and ventral striatum,
171 and subsequent FISH labeling of markers from differential gene analysis (Fig. 2c, 3-5). The
172 clusters corresponded to D1- and D2-MSNs in the matrix, D1- and D2-MSNs in striosome, D1-
173 and D2-MSNs in the NAc shell, and MSN-like neurons located in the interface islands (Fig.
174 2c,d). One cluster was enriched with *DRD1*, *DRD2*, and *CASZ1* and therefore likely
175 corresponded to a hybrid MSN type previously described in rodents (D1H or eccentric-SPN)
176 (Saunders et al., 2018; Stanley et al., 2019). Each MSN subtype cluster was signified by groups
177 of differentially expressed genes that were specifically enriched in that cluster (Fig. 2e, and
178 Table S2). Thus, snRNA-Seq indicates that there are MSN-like subtypes that correspond to the
179 major organizational features of the striatum.
180

Dorsal Striatum

We used FISH to explore the anatomical distribution of MSN subtypes in the dorsal striatum. To establish a baseline, we double-labeled whole coronal sections with *DRD1* and *DRD2* FISH probes (Fig. 3a). As exprected, the majority of neurons expressed either *DRD1* or *DRD2* (Fig. 3b). We counted 325 ± 99 *DRD1*-expressing nuclei/mm^2, and 320 ± 99 *DRD2*-expressing nuclei/mm^2 (Fig. S4a, Fig. 3c). These data illustrate the distribution of the two main classes of MSNs in the NHP striatum. Furthermore, the agreement of our MSN density estimations with previos studies is validation for our methods (Aubert et al., 2000).

Next, we aimed to highlight MSN subtypes in the striosome and matrix compartments. D1-MSN nuclei derived from the dorsal striatum split into one larger cluster and one smaller cluster. Likewise, D2-MSN nuclei derived from the dorsal striatum split into one larger cluster and one smaller cluster. As the matrix compartment has much greater volume than the striosome compartment (Gimenez-Amaya and Graybiel, 1991; Mikula et al., 2009),

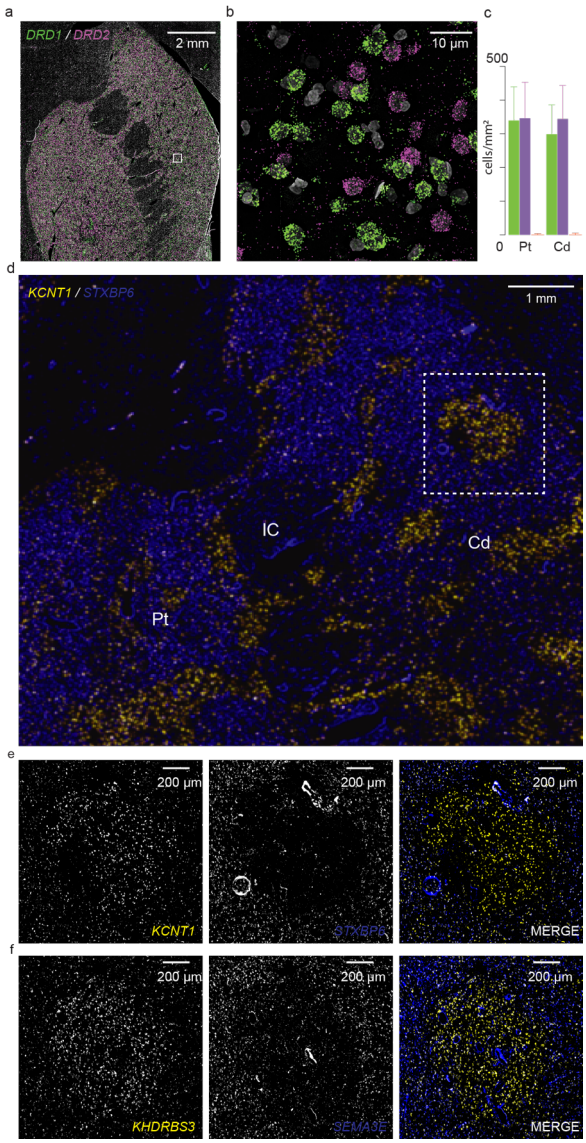

Figure 3. Dorsal Striatum: (a) FISH labeling of *DRD1* (green) and *DRD2* (magenta). White box indicates the ROI shown in **b**. **(b)** High resolution image of region highlighted in **a**. **(c)** Quantification of cell density of neurons expressing *DRD1* (green), *DRD2* (magenta), or both (orange) in the caudate and putamen. Error bars are SD across ROIs. **(d)** FISH labeling of *KCNT1* (yellow) and *STXBP6* (blue) distinguishes striosome and matrix, respectively. **(e)** Detail of the white square in **d**. **(f)** As in **e**, for characteristic striosome and matrix markers, *KHDRBS3* and *SEMA3A.* Scale bars are indicated on images. Abbreviations: Cd, caudate; Pt, putamen; IC, internal capsule.

206 we reasoned that the larger D1- and D2-MSN clusters corresponded to the matrix (Fig. 2a, dark
207 and light blue clusters, respectively), whereas the smaller clusters corresponded to D1- and D2-
208 MSNs in striosome (Fig. 2a, light and dark red clusters, respectively). We identified marker
209 genes for striosome and matrix compartments, each of which included D1- and D2-MSNs. The
210 genes most enriched in NHP striosomes were *KCNT1*, *KHDRBS3*, *FAM163A*, *BACH2*, and
211 *KCNIP1*. The genes most enriched in NHP matrix were *EPHA4, GDA*, *STXBP6*, and *SEMA3E*
212 (Fig. 2e, S4b). Further analysis revealed cell type-specific markers within the striosome
213 compartment – *PDYN* was specifically enriched with striosome D1-MSNs, and *POU6F2* was
214 specifically enriched in striosome D2-MSNs (Fig. S4b). To verify our analysis, we performed
215 double FISH labeling with two potential marker genes, one from striosome and one from matrix.
216 Labeling with *KCNT1* and *STXBP6* showed the characteristic, large-scale pattern of the
217 striosome and matrix compartments (Fig 3d,e), and similar results were obtained for other
218 markers (Fig 3f, S4c). Together, these results highlight marker genes for striosome and matrix
219 compartments of the NHP striatum, and indicate potential molecular access points for achieving
220 cell type specific transgenesis in wild-type subjects.
221
222 ***Ventral Striatum***
223 Four MSN clusters were highly enriched with nuclei from the ventral striatum (Fig. 2d).
224 Three of the clusters were *DRD1* positive, whereas the fourth cluster was *DRD2* positive.
225 Differential gene analysis of the two largest clusters (Fig. 2a, light and dark green) revealed
226 selectively enriched marker genes, including *GREB1L*, *ARHGAP6*, and *GRIA4* (Fig. 2e. Fig.
227 S5a). Double FISH labeling of the striatum with *DRD1* and *ARHGAP6* revealed that *ARHGAP6*
228 was selectively enriched in the most ventral portion of the ventral striatum, a region that
229 corresponds to the NAc shell (Fig. 4a-d). To confirm this finding, we performed double FISH
230 labeling with DRD1 and *GREB1L* and an immunofluorescence stain for calbindin on an adjacent

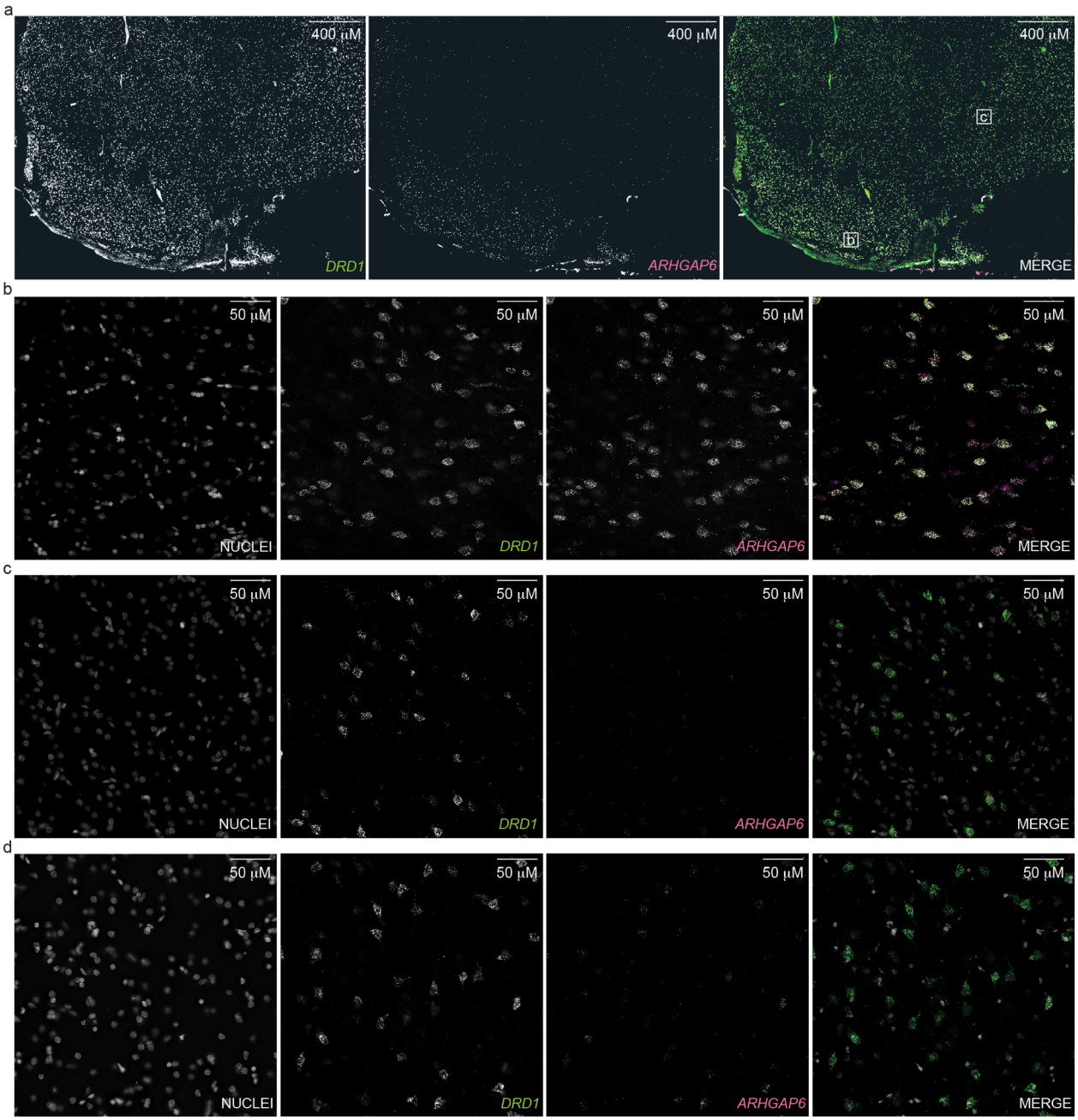

Figure 4. Gene marker enriched in NAc Shell. (a) Double labeling with *DRD1* (left) and *ARHGAP6* (middle) of the NAs shell shows that *ARHGAP6* is selectively enriched in the shell. Lettered boxes indicated ROIs shown in **b**-**c**. **(b)** High-resolution image of the ROI indicated with the letter "b" in **a**, left. **(c)** As in **b**, for ROI indicated with letter "c". **(d)** As in **b**, for an ROI located in the putamen

231 section. Calbindin marks the boundary of the NAc shell (Meredith et al., 1996). The *GREB1L*

232 intensity was similar to the *ARHGAP6* intensity and traced the outline of the transition from the

233 calbindin-poor shell to the calbinin rich core (Fig. S5c,d). There were a significant number of

234 ventral striatum D1- and D2-MSNs that clustered together with D1- and D2-MSNs derived from
235 the matrix compartment of the dorsal striatum. These MSNs may correspond to the 'core'
236 territory, however futher analysis is needed to confirm.

237 One of the most remarkable features of the *DRD1* and *DRD2* labelling of the striatum
238 was the presence of discrete 'islands' in the ventral striatum that included many *DRD1*-positive
239 cells, but few to no *DRD2*-positive cells (Fig. 5a). We wondered whether these D1-exclusive
240 islands corresponded the two small clusters derived from the ventral striatum (Fig. 2a, light and
241 dark orange). Both clusters expressed many markers commonly associated with MSNs (Fig.
242 5b). Nevertheless, both clusters where characterized by sets of differentially expressed genes
243 specifically enriched in each cluster (Fig. 2c). *RXFP1* and *CPNE4* were two of the most
244 selective genes for these two respective clusters (Fig. 5b). We used FISH probes directed at
245 *RXFP1* and *CPNE4*, together with the *DRD1* probe to triple-label the striatum (Fig. 5c). Triple-
246 labeling with *DRD1*, *RXFP1*, and *CPNE4* probes on one coronal section revealed that *RXFP1*
247 and *CPNE4* probes labeled distinct D1-exclusive cell islands (Fig. 5c). High resolution confocal
248 scanning microscopy verified that *RXFP1* and *DRD1* colocalized in the same cells in one island
249 (Fig. 5d), whereas *CPNE4* and *DRD1* colocalized in the same cells of another island (Fig. 5e).
250 Triple labeling outside of the D1-exclusive islands revealed no detectable co-localization
251 between *DRD1* and *CPNE4***.** Likewise, outside of the D1-exclusive islands, we observed only
252 rare *DRD1* and *RXFP1* colocalizations in nuclei that might correspond with "D1H" or "eSPN"
253 cells (Fig. 5f) (Saunders et al., 2018; Stanley et al., 2019). These results suggested that the
254 *RXFP1* positive and *CPNE4* positive MSN subtypes are located in distinct anatomical islands
255 within the ventral striatum.

256 To determine how these types of D1-exclusive islands were distributed throughout the
257 striatum, we performed the triple *DRD1*, *RXFP1*, and *CPNE4* FISH labeling on five coronal
258 sections distributed along the rostro-caudal axis (Fig. 5g). We defined the caudal and ventral
259 borders of the NAc by comparison of Nissl stained sections with a high-resolution MRI and DTI

Rhesus macaque brain atlas, and we mapped all clusters within and near the borders of the ventral striatum (Bakker et al., 2015; Calabrese et al., 2015). The *CPNE4* positive islands corresponded with the Islands of Calleja (ICj) and the olfactory tubercle; this was verified by strong *CPNE4* and *DRD1* colocalization in the major Island of Celleja (mICj). Correspondingly, visual inspection of these clusters under Nissl staining revealed many of these cells to be granule cells. The *RXFP1* islands, on the other hand, had larger nuclei that were less densely packed together. Cells within these islands co-expressed *DRD1*, *RXFP1*, and high levels of *OPRM1*, the gene for the mu-opioid receptor (Fig. 5b). Triple labeling of *DRD1*, *DRD2* and *RXFP1* confirmed that cells in these cluster exclusively express *DRD1* and not *DRD2* (Fig S6b). Moreover, *RXFP1* islands were not restricted to the border of the NAc, as are ICjs. Rather they were found throughout the NAc and even in the putamen (Fig. 5g, orange arrows, S6a). For these reasons, we concluded that these *RXFP1* positive cell type islands likely corresponded with “Neurochemically Unique Domains in the Accumbens and Putamen (NUDAPs)”(Daunais et al., 2001; Voorn et al., 1996). Using colocalization of *DRD1* and *RXFP1*, we observed NUDAPs to the caudal extent of the NAc (Fig. 5h, orange arrows). FISH labeling verified these clusters in a second Rhesus monkey (Fig. S6c). Therefore, *RXFP1* positive islands represent a persistent feature of the ventral striatum.

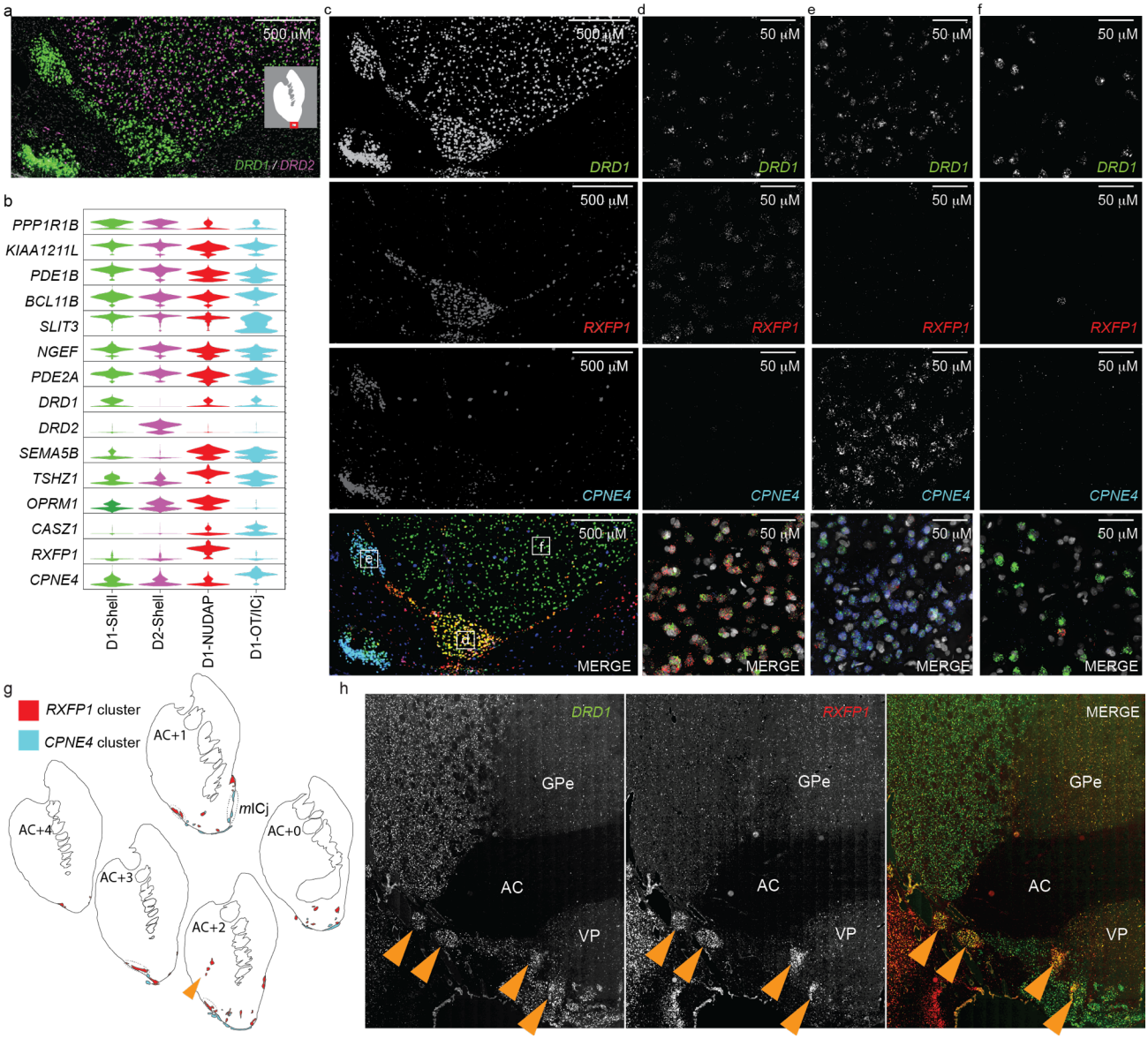

Figure 5. MSNs in the interface islands. (a) FISH stain of *DRD1* (green) and *DRD2* (magenta) highlights *DRD1* exclusive islands. Inset, White area indicates striatum and the red box highlights the area shown in **a** and **c**. **(b)** Violin plots of relevant marker genes in ventral striatum MSN subtypes. **(c)** FISH stain of *DRD1* (top), *RXFP1* (middle top) and *CPNE4* (middle bottom) and merged channels (bottom) on immediately adjacent section shown in **a**. **(d-f)** Maximum intensity projections (MIP) from high-resolution confocal images of the three locations indicated in **c**, bottom. Colors and order as in **c**. **(g)** Distribution of *RXFP1* and *CPNE4* clusters across five rostral-caudal regions identified by multichannel FISH. AC = anterior commissure, mICj = major Island of Calleja. **(h)** Caudal section (AC-1) of triple labeled NHP striatum shows four *RXFP1* positive clusters, indicated by orange arrows, that fall within the most caudal potion of the NAc. Note, at this level we observed no ICjs, so the *CPNE4* channel is not shown. Abbreviations: AC, anterior commissure; GPe, External portion of the Globus Pallidus; VP, Ventral Pallidum.

280 **Discussion**

281 Here we investigated the cell type-specific structure of the Rhesus macaque striatum with a
282 primary focus on the transcriptional and anatomical diversity among MSN and MSN-like
283 neurons. snRNA-Seq revealed a clear distinction between MSN subtypes located in the dorsal
284 and ventral striatum. The dorsal striatum included MSN subtypes specific to the striosome and
285 matrix compartments (Fig. 2a). We found marker genes, including *BACH2* and *KCNT2*
286 (Fig. 2e,3), that were expressed in all striosome MSNs, but we also found markers for
287 compartment-specific cell types, including *PDYN* and *POU6F2* that were enriched in D1- and
288 D2-Striosome MSNs, respectively. The ventral striatum also yielded distinct MSN clusters. Two
289 of the clusters corresponded to D1- and D2-MSNs located in the NAc shell (Fig 2a, 4).
290 Transcriptional and FISH analysis of the other two clusters revealed them to be associated with
291 the 'interface islands' – dense cellular islands located within and near the ventral border of the
292 striatum. One of those clusters was highly enriched with *CPNE4* and strongly labeled the
293 Islands of Calleja and the olfactory tubercle. The D1-MSN cluster marked by expression of
294 *RXFP1* mapped to NUDAPs, regions previously identified in human and NHP NAc and putamen
295 via mu-opioid receptor ligand binding (Daunais et al., 2001; Voorn et al., 1996). Together, these
296 cell types provide a roadmap for studying cell type-specific functions during sophisticated
297 primate behaviors, and the cell type specific marker genes define potential molecular access
298 points to enable the application of genetically coded tools in scientific or translational contexts.

299 Each of the MSN subtypes had differentially expressed genes that were specifically
300 enriched in each cluster (Fig. 2c, e and Table S2). Gene functional analyses revealed that all
301 MSN subtypes were enriched with similar gene pathways that support well known MSN
302 functions. These included gene pathways related to neuropeptide signaling, ion channels, and
303 synaptic transmission. However, within each of these gene pathways, the MSN subtypes
304 showed specialized expression of unique gene pathway members, providing possible molecular
305 evidence for functional divergence between MSN subtypes. Most notably, the *RXFP1* positive

306 subtype, restricted to NUDAPs, was enriched with genes known to serve a host of critical striatal
307 processes ranging from LTD and LTP to pain and anxiety. Together with enhanced expression
308 of *OPRM1* and other reward- and learning-related genes, these results suggest that these
309 structures have a role in reward processing and perhaps even drug addiction. Future studies
310 using the latest genetically coded calcium sensors and chemical actuators will be required to
311 properly appreciate this prominent feature of primate basal forebrain.

312 This study and others demonstrate that single cell technologies can be effectively
313 applied to NHPs (Krienen et al., 2020; Zhu et al., 2018). We foresee at least three critical
314 reasons to avidly apply single cell technologies to NHP. (1) Old-world monkeys like Rhesus
315 macaques are more similar to humans than any other research animal that allows for invasive
316 neurophysiological experiments. Accordingly, Rhesus macaque cell types, including highly
317 specialized neurons like Betz cells, von Economo neurons, and even striatal interneuron
318 subtypes recapitulate homologous human cell types better than cells from rodents or even from
319 marmosets (Bakken et al., 2020; Evrard et al., 2012; Krienen et al., 2020). (2) Single cell studies
320 performed on post-mortem human tissue are subject to ethical constraints that manifest as
321 relatively long and highly variable postmortem intervals (PMIs) (Hodge et al., 2019). In contrast,
322 NHP experiments can be performed in a highly controlled fashion. (3) NHPs have resisted the
323 widespread application of modern genetically coded tools. Single cell technologies, including
324 RNA-Seq and ATAC-Seq, can identify atomized cell types and potent regulatory sequences that
325 will break this resistance and enable the effective applications of genetically coded tools in
326 large, wild type animals that resemble humans. Thus, the application of single cell technologies
327 will propel Rhesus macaque systems neuroscience studies into the genomics era by
328 discovering and describing the molecular properties of the primate brain, reveal unknown (or
329 incompletely known) cell types, and pinpoint cell type- and circuit-specific molecular access
330 points to enable scientific and clinical application of genetically coded tools.

Rhesus macaque behavior is readily interpretable in terms of human behavioral theory such as economic theory (Genest et al., 2016; Lak et al., 2014; Stauffer et al., 2015; Stauffer et al., 2014), learning theory (Waelti et al., 2001), and even game theory (Barraclough et al., 2004; Haroush and Williams, 2015). Our ultimate goal is to understand the cell type-specific neural computations that underlie these sophisticated behaviors. The diversity of MSN cell types presented here provides a blueprint to achieve this level of understanding for striatal functions in primates.

339 **Methods**

340 ***Subjects and surgery:*** All animal procedures were in accordance with the National Institutes of
341 Health Guide for the Care and Use of Laboratory Animals and approved by the University of
342 Pittsburgh's Institutional Animal Care and Use Committee (IACUC) (Protocol ID, 19024431).
343 Rhesus Monkeys were single- or pair-housed with a 12h-12h light-dark cycle. Monkey F was a
344 12-year-old female (8.1 kg). Monkey P was a 5-year-old female (5.4kg). Monkey B was a 13-
345 year-old male (11.78 kg). Monkey K was a 4-year-old male (6.0 kg). For MRI, we anesthetized
346 monkey F and P with ketamine and maintained general anesthesia with isoflurane. We head
347 fixed the monkeys using a MRI-compatible stereotaxic frame and scanned (Siemens, 3T) for
348 anatomical MRI. We generated a whole brain model for each monkey using Brainsight (Rogue
349 Research) and 3-D printed a custom matrix for the brain with cutting guide set every 1 mm.

350 To maximize nuclei viability, we followed a harvesting protocol similar to the one outlined
351 in Davenport et al. (2014). Briefly, animals were initially sedated with ketamine (15 mg/kg IM),
352 and then ventilated and further anesthetized with isoflurane. The animals were transported to a
353 surgery suite and placed in a stereotaxic frame (Kopf Instruments). We removed the calvarium
354 and then perfused the circulatory systems with 3-4 liters of ice cold artificial cerebrospinal fluid
355 (ACSF; 124 mM NaCl, 5 mM KCl, 2 mM $MgSO_4$, 2 mM $CaCl_2$, 23 mM $NaHCO_3$, 3 mM
356 NaH_2PO_4, 10 mM glucose; pH 7.4, osmolarity 290–300 mOsm) oxygenated with 95 % O_2:5 %
357 CO_2. We then opened the dura and removed the brain. We sliced on the custom brain matrix
358 into 4 mm slabs. We removed three striatal regions – the caudate, putamen, and ventral
359 striatum –under a dissection microscope for nuclei isolation. Monkeys B and K, for FISH, were
360 perfused with 4% paraformaldehyde (PFA, Sigma-Aldrich P6148) in phosphate buffered saline
361 (PBS, Fisher scientific BP243820) supplemented with 10% sucrose (Sigma-Aldrich S8501). The
362 brain was post-fixed with 4% PFA and cryopreserved with a gradient of sucrose (10%, 20%,
363 30%) in PBS.

364

365 ***Nuclei isolation:*** We isolated nuclei isolated as previously described (Habib et al., 2017).
366 Briefly, we homogenized tissues using a loose glass dounce homogenizer followed by a tight
367 glass homogenizer in EZ PREP buffer (Millipore Sigma, NUC-101). We washed nuclei once with
368 EZ PREP buffer and once with Nuclei Suspension Buffer (NSB; consisting of 1× PBS, 0.01%
369 BSA and 0.1% RNase inhibitor (Clontech, Cat #2313A)). We re-suspended the washed nuclei in
370 NSB and filtered them through a 35-μm cell strainer (Corning, Cat # 352235). We counted the
371 nuclei and diluted down to 1000 cells/μl. We loaded approximately 10,000 cells from each brain
372 region onto a 10X chip and run through a 10x Genomics Chromium controller.
373
374 ***Single nucleus RNA-Seq***: We used 10x Chromium Single Cell 3' Reagent kits v3 Chemistry for
375 monkeys F and P. We reverse transcribed RNAs and generated libraries according to 10x
376 Genomics protocol. Briefly, we generated Gel beads-in-emulsion (GEMs) after running through
377 a 10x Genomics Chromium controller. We reverse transcribed mRNAs within GEMs in a Bio-
378 Rad PCR machine (C1000). We barcoded cDNAs from individual cells with 10x Genomics
379 Barcodes and barcoded different transcripts with unique molecular identifiers (UMIs). We
380 purified cDNAs with Dynabeads (10x Genomics, 2000048) after breaking the emulsion with a
381 recovery agent (10x Genomics, 220016). Then, we amplified cDNAs by PCR and purified them
382 with SPRIselect reagent (Beckman Coulter, B23318). We analyzed the cDNA quantification and
383 quality using Agilent Bioanalyzer 2100. We prepared libraries following fragmentation, end
384 repair, A-tailing, adaptor ligation, and sample index PCR. We quantified the libraries by qPCR
385 using KAPA Library Quantification Kit (KAPA Biosystems, KK4824). We pooled together
386 libraries from individual monkeys and loaded them onto NovaSeq S4 Flow Cell Chip. We
387 sequenced samples from monkeys F and P to depths of 400,000 and 250,000 reads per nuclei,
388 respectively.
389

390 ***Custom annotation file***: We downloaded the macaque rheMac10 genome
391 (https://hgdownload.soe.ucsc.edu/goldenPath/rheMac10/bigZips/rheMac10.fa.gz) and human
392 NCBI RefSeq transcriptome annotation gtf file from the UCSC genome browser
393 (https://hgdownload.soe.ucsc.edu/goldenPath/hg38/bigZips/genes/hg38.ncbiRefSeq.gtf.gz). We
394 used the UCSC liftOver tool with the hg38toRheMac10 chain file
395 (https://hgdownload.soe.ucsc.edu/goldenPath/hg38/liftOver/hg38ToRheMac10.over.chain.gz) to
396 liftOver the human transcriptome gtf file onto the rheMac10 genome, with a minimal match
397 threshold of 0.85. We then used this new gtf in the alignment of the 10x reads to the macaque
398 genome.
399
400 ***Data Analysis:*** We performed exploratory analysis of striatum samples in monkey F. We
401 converted raw illumina signal bcl to fastq files using the Cell Ranger suite, then aligned to the
402 rheMac10 genome using the STAR aligner with the -solo option for single cell demultiplexing
403 and using the custom rheMac10 gtf as above. We removed empty droplets with the dropletUtils
404 *defaultDrops* function (Griffiths et al., 2018), and removed doublets using the *SCDS* hybrid
405 doublet caller with a threshold of 1.0 (Bais and Kostka, 2020). We performed pre-clustering
406 using Scanpy's Leiden clustering function with low quality cells removed based on gene count
407 with cluster-specific parameters (Wolf et al., 2018). We normalized single cell gene expression
408 values using the *scran* size factor normalization method, with our pre-clustering as input to the
409 function (Lun et al., 2016). After expression count normalization, we used Scanpy's highly
410 variable genes function to select the top 7500 highly variable genes in the dataset. We
411 performed an iterative principal component analysis (PCA) using the highly variable genes from
412 nearest neighbor graphs with Scanpy's *neighbors* function. We used Leiden clustering of the
413 resulting neighbor graphs to distinguish major cell types, i.e. medium spiny neurons. We re-run
414 Leiden clustering for medium spiny neurons specifically, resulting in several robust D1 neuronal
415 types.

416 To further validate the reproducibility of monkey F' cell types in monkey P, we used
417 Seurat v3 pipeline to perform an integrated analysis of monkeys F and P. First, we removed
418 ambient RNA in monkey P using SoupX (Young and Behjati, 2020). Neuronal cells express
419 higher numbers of genes compared to non-neuronal cells (Hodge et al., 2019; Tasic et al.,
420 2018; Zeisel et al., 2018) and therefore we used two different thresholds to remove low quality
421 neuronal and non-neuronal nuclei. We chose these thresholds as the minimal level that
422 produced clear cluster separation (Fig. 1e). We then deleted ribosomal genes for both monkeys,
423 and removed doublets using DoubletDetection (McGinnis et al., 2019). We performed standard
424 log-normalization and a variance stabilizing transformation prior to finding anchors, and
425 identified variable features individually for each monkeys' data set using Seurat's
426 *FindVariableFeatures* function. Next, we identified anchors using the
427 *FindIntegrationAnchors* function with default parameters and passed these anchors to
428 the IntegrateData function. This returned a Seurat object with an integrated expression matrix
429 for all nuclei. We scaled the integrated data, ran PCA, and visualized the results with UMAP.
430 We clustered the cells based on Louvain clustering and chose resolution that reflected the major
431 cell classes of striatum including D1- and D2- MSNs, interneurons and astrocytes. We
432 annotated the clusters based on feature plots of well-known marker genes and verified the
433 identities of cell clusters by hypergeometric test based on their differentially expressed genes. In
434 order to analyze MSNs in detail, we extracted MSN nuclei. We randomly sampled MSN nuclei
435 from monkey P in order to balance the sample size for each monkey. We the re-calculated
436 principle components (PCs) and performed UMAP dimensionality reduction on the first 15 PCs.
437 We used Louvain clustering to cluster the MSNs. We chose a resolution that reflected the main
438 functional divisions in the striatum, including direct and indirect pathways, striosome and matrix
439 compartments, and core and shell territories.
440

441 ***FISH:*** We designed FISH probes to validate direct- and indirect- pathways and NAc-enriched
442 MSN cell types, as follows: *DRD1* (#549041, NM_001206975.1), *DRD2* (#549031-C2,
443 XM_001085571.3), *RXFP1* (#801121-C2, XM_001096574.4), *CPNE4* (#801111-C3,
444 XM_028843706.1), *KCNT1* (#881571-C3, XM_015116381.2), *KHDRBS3* (#881591-C3,
445 XM_028852934.1), *STXBP6* (#881611-C2, NM_001260925.1), *SEMA3E* (#879971-C2,
446 XM_028846126.1), *GREB1L* (#898991-C3, XM_015121640.2), *ARHGAP6* (#898981-C3,
447 XM_001094565.3).
448 We embedded brains in optimal cutting temperature (OCT) and stored them at -80°C
449 until cutting. We cut floating sections at 15 and 30 μm, in monkey B and K, respectively,
450 mounted tissue on 2x3" pre-treated slides, and preserved the slides in a freezer at -80°C. We
451 used the Advanced Cell Diagnostics (ACD) RNAscope platform and Multiplex Fluorescent
452 Detection Reagents v2 to perform FISH with slight modifications for monkey brain. Briefly, we
453 air dried slides for 30 min after removal from -80°C freezer and baked them at 60°C for 20 min.
454 We treated the brain sections with hydrogen peroxide (ACD, 322335) for 10 min at room
455 temperature and then with RNAscope Target Retrieval Reagents (ACD, 322000) for 8 min at
456 99°C. We incubated the slides in 100% alcohol for 3 min and then dried them in 60°C for 10
457 min. We then treated the samples with protease III (ACD, 322337) for 30 min at 40°C and
458 incubated them with probes for 2 hr. After hybridization with AMP 1, 2 and 3, we included the
459 slides with different HRP channels and fluorophores, including Opal 520 (PerkinElmer,
460 FP1487A), Opal 570 (PerkinElmer, FP1488A) and Opal 650 (PerkinElmer, FP1496A). We used
461 Trublack (Biotium, 23007) to quench Lipofuscin autofluorescence for 45 s at room temperature.
462 We counterstained every slide with DAPI and mounted with Prolong Gold Antifade Mountant
463 (Life technologies, P36930).
464 We scanned labeled sections using a Hamamatsu NanoZoomer S360 or a Nikon Eclipse
465 T*i*2 under 20x objective. For high resolution images, we used a Nikon Eclipse T*i*2 or an
466 Olympus IX83 under 40x or 63x objective. We took multi-layer images and used maximum

467 intensity projections to create single images. We used NDP software to convert original file
468 scanned by NanoZoomer to tiff format and ImageJ and Adobe Photoshop to adjust brightness
469 and overlay images.

470 To quantify cells expressing *DRD1* and *DRD2* in the caudate and putamen (Fig. S4a),
471 we chose ten representative areas from each striatal region. Through visual inspection, we
472 identified cells containing three or more puncta as positive for that gene. We quantified the total
473 number of *DRD1*-positive and *DRD2*-positive cells for each striatal region of interest (ROI), in
474 each section and counted positive cells on three rostro-caudal sections. We calculated cell
475 density as the number of positive cells divided by total number of nuclei in the area.

476

477 ***D1 islands mapping***: In order to map the distribution of D1-RXFP1 and D1- CPNE4 islands, we
478 triple labeled five sections spaced at 750 mm intervals with probes against *DRD1*, *RXFP1*, and
479 *CPNE4*. We scanned the whole sections and ran a custom CellProfiler pipeline (Carpenter et
480 al., 2006) to determine the spatial distribution of nuclei and signal intensity of individual channel
481 for each nucleus. We marked regions as D1-RXFP1 (D1-CPNE4) that had a majority of cells
482 double-labeled with *DRD1* and *RXFP1* (*CPNE4*). To confirm that these islands were D1
483 exclusive, we double-labeled sections with *DRD1* and *DRD2* adjacent to the above five
484 sections. We confirmed that these islands are exclusively the D1 clusters from the similar
485 CellProfiler analysis.

486
487
488 **Supplementary Figure Legends**

489 **Fig. S1 Read mapping.** Comparison of gene mapping rate using four different gtf in our
490 alignment of reads to macaque genome. We used UCSC liftOver tool to liftOver the human
491 transcriptome gtf file onto the rheMac8 or rheMac10 genome to get liftOver version
492 rheMac8_liftOver and rheMac10_liftOver, respectively.

493

494 **Fig. S2. Marker Genes. (a-e)** Feature plots of marker gene expression for major cell classes in
495 striatal nuclei.
496
497 **Fig. S3. MSN comparisons**. **(a)** Feature plot showing the expression of *RBFOX3*, which labels
498 all neurons. **(b-h)** Feature plots of gene expression for well-known MSN markers, *PPP1R1B*
499 and *BCL11B*, *PDE1B* and new MSN-specific markers, *KIAA1211L*, *PDE2A*, *SLIT3*, *NGEF*. **(i)**
500 Standard deviation in different principal components (PCs). The first 15 PCs account for
501 majority of the variation. **(j)** Side by side monkey comparison for MSNs in UMAP coordinates.
502 (**k**) UMAP visualization of MSNs colored by three regions.
503
504 **Fig. S4. Dorsal striatum**. **(a)** Schematic diagrams of the three sections used for *DRD1* and
505 *DRD2* quantification. The square boxes indicated the quantified ROIs. **(b)** Violin plots of
506 striosome (yellow) and matrix (blue) marker gene expression in MSNs. **(c)** FISH labeling of
507 *KHDRBS3* (yellow) and *SEMA3E* (blue). Scale bars are indicated on the images.
508
509 **Fig. S5. Ventral Striatum. (a)** Feature plots for NAc shell markers. **(b)** DARPP32
510 immunohistochemistry identifies the borders of the striatum. **(c)** Calbindin
511 immunohistochemistry reveals the border between the core and shell, highlighted by yellow
512 arrows. **(d)** Double FISH labelling with *DRD1* and *GREB1L*. (left) *GREB1L* intensity follows the
513 border of the shell, indicated by the yellow arrows. (right) *DRD1* (green) and *GREB1L*
514 (magenta) merged.
515
516 **Fig. S6. Interface islands. (a)** Identification of *RXFP1* islands in putamen. Left image shows a
517 schematic of *RXFP1* islands in the putamen and right image shows FISH stain of *DRD1* (green),
518 *RXFP1* (red) and *CPNE4* (blue). Nuclei labeled by DAPI (grey). **(b)** Triple label FISH of *DRD1*
519 (green), *RXFP1* (red) and *DRD2* (blue) shows that *RXFP1* islands do not express *DRD2*. Nuclei

520 labeled by DAPI (grey). **(c)** Identification of *RXFP1* and *CPNE4* islands in a second monkey
521 (monkey K). FISH stain of *DRD1* (green), *RXFP1* (red) and *CPNE4* (blue). Nuclei labeled by
522 DAPI (grey). These images show representative *CPNE4* and *RXFP1* clusters in NAc. Scale
523 bars are indicated on the images.
524

References

Albin, R.L., Young, A.B., and Penney, J.B. (1989). The functional anatomy of basal ganglia disorders. Trends Neurosci *12*, 366-375.

Arlotta, P., Molyneaux, B.J., Jabaudon, D., Yoshida, Y., and Macklis, J.D. (2008). Ctip2 controls the differentiation of medium spiny neurons and the establishment of the cellular architecture of the striatum. J Neurosci *28*, 622-632.

Aubert, I., Ghorayeb, I., Normand, E., and Bloch, B. (2000). Phenotypical characterization of the neurons expressing the D1 and D2 dopamine receptors in the monkey striatum. J Comp Neurol *418*, 22-32.

Bais, A.S., and Kostka, D. (2020). scds: computational annotation of doublets in single-cell RNA sequencing data. Bioinformatics *36*, 1150-1158.

Bakken, T.E., Jorstad, N.L., Hu, Q., Lake, B.B., Tian, W., Kalmbach, B.E., Crow, M., Hodge, R.D., Krienen, F.M., Sorensen, S.A.*, et al.* (2020). Evolution of cellular diversity in primary motor cortex of human, marmoset monkey, and mouse. bioRxiv, 2020.2003.2031.016972.

Bakker, R., Tiesinga, P., and Kötter, R. (2015). The Scalable Brain Atlas: Instant Web-Based Access to Public Brain Atlases and Related Content. Neuroinformatics *13*, 353-366.

Barraclough, D.J., Conroy, M.L., and Lee, D. (2004). Prefrontal cortex and decision making in a mixed-strategy game. Nat Neurosci *7*, 404-410.

Calabrese, E., Badea, A., Coe, C.L., Lubach, G.R., Shi, Y., Styner, M.A., and Johnson, G.A. (2015). A diffusion tensor MRI atlas of the postmortem rhesus macaque brain. NeuroImage *117*, 408-416.

Carpenter, A.E., Jones, T.R., Lamprecht, M.R., Clarke, C., Kang, I.H., Friman, O., Guertin, D.A., Chang, J.H., Lindquist, R.A., Moffat, J.*, et al.* (2006). CellProfiler: image analysis software for identifying and quantifying cell phenotypes. Genome Biol *7*, R100.

Crittenden, J., and Graybiel, A. (2011). Basal Ganglia Disorders Associated with Imbalances in the Striatal Striosome and Matrix Compartments. Frontiers in Neuroanatomy *5*, 59.

Daunais, J.B., Letchworth, S.R., Sim-Selley, L.J., Smith, H.R., Childers, S.R., and Porrino, L.J. (2001). Functional and anatomical localization of mu opioid receptors in the striatum, amygdala, and extended amygdala of the nonhuman primate. J Comp Neurol *433*, 471-485.

Davenport, A.T., Grant, K.A., Szeliga, K.T., Friedman, D.P., and Daunais, J.B. (2014). Standardized method for the harvest of nonhuman primate tissue optimized for multiple modes of analyses. Cell Tissue Bank *15*, 99-110.

DeLong, M.R., and Wichmann, T. (2015). Basal Ganglia Circuits as Targets for Neuromodulation in Parkinson Disease. JAMA Neurol *72*, 1354-1360.

DiFiglia, M., Pasik, P., and Pasik, T. (1976). A Golgi study of neuronal types in the neostriatum of monkeys. Brain Research *114*, 245-256.

Evrard, H.C., Forro, T., and Logothetis, N.K. (2012). Von Economo neurons in the anterior insula of the macaque monkey. Neuron *74*, 482-489.

Floresco, S.B. (2015). The nucleus accumbens: an interface between cognition, emotion, and action. Annu Rev Psychol *66*, 25-52.

Genest, W., Stauffer, W.R., and Schultz, W. (2016). Utility functions predict variance and skewness risk preferences in monkeys. Proc Natl Acad Sci U S A *113*, 8402-8407.

Gerfen, C.R. (1984). The neostriatal mosaic: compartmentalization of corticostriatal input and striatonigral output systems. Nature *311*, 461-464.

Gimenez-Amaya, J.M., and Graybiel, A.M. (1991). Modular organization of projection neurons in the matrix compartment of the primate striatum. The Journal of Neuroscience *11*, 779.

571 Gokce, O., Stanley, Geoffrey M., Treutlein, B., Neff, Norma F., Camp, J.G., Malenka, Robert C.,
572 Rothwell, Patrick E., Fuccillo, Marc V., Südhof, Thomas C., and Quake, Stephen R. (2016).
573 Cellular Taxonomy of the Mouse Striatum as Revealed by Single-Cell RNA-Seq. Cell Reports
574 *16*, 1126-1137.
575 Graybiel, A.M., and Ragsdale, C.W., Jr. (1978). Histochemically distinct compartments in the
576 striatum of human, monkeys, and cat demonstrated by acetylthiocholinesterase staining. Proc
577 Natl Acad Sci U S A *75*, 5723-5726.
578 Griffiths, J.A., Richard, A.C., Bach, K., Lun, A.T.L., and Marioni, J.C. (2018). Detection and
579 removal of barcode swapping in single-cell RNA-seq data. Nat Commun *9*, 2667.
580 Haber, S.N., and McFarland, N.R. (1999). The Concept of the Ventral Striatum in Nonhuman
581 Primates. Annals of the New York Academy of Sciences *877*, 33-48.
582 Habib, N., Avraham-Davidi, I., Basu, A., Burks, T., Shekhar, K., Hofree, M., Choudhury, S.R.,
583 Aguet, F., Gelfand, E., Ardlie, K.*, et al.* (2017). Massively parallel single-nucleus RNA-seq with
584 DroNc-seq. Nature Methods *14*, 955.
585 Haroush, K., and Williams, Ziv M. (2015). Neuronal Prediction of Opponents Behavior during
586 Cooperative Social Interchange in Primates. Cell *160*, 1233-1245.
587 Heimer, L., and Wilson, R. (1975). The subcortical projections of allocortex: similarities in the
588 neuronal associations of the hippocampus, the piriform cortex and the neocortex. Paper presented
589 at: Golgi centennial symposium proceedings (Raven).
590 Hodge, R.D., Bakken, T.E., Miller, J.A., Smith, K.A., Barkan, E.R., Graybuck, L.T., Close, J.L.,
591 Long, B., Johansen, N., Penn, O.*, et al.* (2019). Conserved cell types with divergent features in
592 human versus mouse cortex. Nature *573*, 61-68.
593 Hong, S., Amemori, S., Chung, E., Gibson, D.J., Amemori, K.-i., and Graybiel, A.M. (2019).
594 Predominant Striatal Input to the Lateral Habenula in Macaques Comes from Striosomes.
595 Current Biology *29*, 51-61.e55.
596 Krienen, F.M., Goldman, M., Zhang, Q., C. H. del Rosario, R., Florio, M., Machold, R.,
597 Saunders, A., Levandowski, K., Zaniewski, H., Schuman, B.*, et al.* (2020). Innovations present
598 in the primate interneuron repertoire. Nature *586*, 262-269.
599 Lak, A., Stauffer, W.R., and Schultz, W. (2014). Dopamine prediction error responses integrate
600 subjective value from different reward dimensions. Proc Natl Acad Sci U S A *111*, 2343-2348.
601 Lee, H., Fenster, R.J., Pineda, S.S., Gibbs, W.S., Mohammadi, S., Davila-Velderrain, J., Garcia,
602 F.J., Therrien, M., Novis, H.S., Gao, F.*, et al.* (2020). Cell Type-Specific Transcriptomics
603 Reveals that Mutant Huntingtin Leads to Mitochondrial RNA Release and Neuronal Innate
604 Immune Activation. Neuron *107*, 891-908.e898.
605 Lun, A.T., Bach, K., and Marioni, J.C. (2016). Pooling across cells to normalize single-cell RNA
606 sequencing data with many zero counts. Genome Biol *17*, 75.
607 Martin, A., Calvigioni, D., Tzortzi, O., Fuzik, J., Warnberg, E., and Meletis, K. (2019). A
608 Spatiomolecular Map of the Striatum. Cell Rep *29*, 4320-4333 e4325.
609 Märtin, A., Calvigioni, D., Tzortzi, O., Fuzik, J., Wärnberg, E., and Meletis, K. (2019). A
610 Spatiomolecular Map of the Striatum. Cell Reports *29*, 4320-4333.e4325.
611 McGinnis, C.S., Murrow, L.M., and Gartner, Z.J. (2019). DoubletFinder: Doublet Detection in
612 Single-Cell RNA Sequencing Data Using Artificial Nearest Neighbors. Cell Syst *8*, 329-337
613 e324.
614 Meredith, G.E., Pattiselanno, A., Groenewegen, H.J., and Haber, S.N. (1996). Shell and core in
615 monkey and human nucleus accumbens identified with antibodies to calbindin-D28k. J Comp
616 Neurol *365*, 628-639.

617 Mikula, S., Parrish, S.K., Trimmer, J.S., and Jones, E.G. (2009). Complete 3D visualization of
618 primate striosomes by KChIP1 immunostaining. Journal of Comparative Neurology *514*, 507-
619 517.
620 Muñoz-Manchado, A.B., Bengtsson Gonzales, C., Zeisel, A., Munguba, H., Bekkouche, B.,
621 Skene, N.G., Lönnerberg, P., Ryge, J., Harris, K.D., Linnarsson, S.*, et al.* (2018). Diversity of
622 Interneurons in the Dorsal Striatum Revealed by Single-Cell RNA Sequencing and PatchSeq.
623 Cell Reports *24*, 2179-2190.e2177.
624 Parent, A., and Hazrati, L.-N. (1995). Functional anatomy of the basal ganglia. I. The cortico-
625 basal ganglia-thalamo-cortical loop. Brain Research Reviews *20*, 91-127.
626 Saunders, A., Macosko, E.Z., Wysoker, A., Goldman, M., Krienen, F.M., de Rivera, H., Bien, E.,
627 Baum, M., Bortolin, L., Wang, S.*, et al.* (2018). Molecular Diversity and Specializations among
628 the Cells of the Adult Mouse Brain. Cell *174*, 1015-1030 e1016.
629 Savell, K.E., Tuscher, J.J., Zipperly, M.E., Duke, C.G., Phillips, R.A., Bauman, A.J., Thukral, S.,
630 Sultan, F.A., Goska, N.A., Ianov, L.*, et al.* (2020). A dopamine-induced gene expression
631 signature regulates neuronal function and cocaine response. Science Advances *6*, eaba4221.
632 Smith, J.B., Klug, J.R., Ross, D.L., Howard, C.D., Hollon, N.G., Ko, V.I., Hoffman, H.,
633 Callaway, E.M., Gerfen, C.R., and Jin, X. (2016). Genetic-Based Dissection Unveils the Inputs
634 and Outputs of Striatal Patch and Matrix Compartments. Neuron *91*, 1069-1084.
635 Stanley, G., Gokce, O., Malenka, R.C., Südhof, T.C., and Quake, S.R. (2019). Continuous and
636 Discrete Neuron Types of the Adult Murine Striatum. Neuron.
637 Stauffer, W.R., Lak, A., Bossaerts, P., and Schultz, W. (2015). Economic choices reveal
638 probability distortion in macaque monkeys. J Neurosci *35*, 3146-3154.
639 Stauffer, W.R., Lak, A., and Schultz, W. (2014). Dopamine reward prediction error responses
640 reflect marginal utility. Curr Biol *24*, 2491-2500.
641 Tang, F., Barbacioru, C., Wang, Y., Nordman, E., Lee, C., Xu, N., Wang, X., Bodeau, J., Tuch,
642 B.B., Siddiqui, A.*, et al.* (2009). mRNA-Seq whole-transcriptome analysis of a single cell.
643 Nature Methods *6*, 377-382.
644 Tasic, B., Yao, Z., Graybuck, L.T., Smith, K.A., Nguyen, T.N., Bertagnolli, D., Goldy, J.,
645 Garren, E., Economo, M.N., Viswanathan, S.*, et al.* (2018). Shared and distinct transcriptomic
646 cell types across neocortical areas. Nature *563*, 72-78.
647 Voorn, P., Brady, L.S., Berendse, H.W., and Richfield, E.K. (1996). Densitometrical analysis of
648 opioid receptor ligand binding in the human striatum--I. Distribution of mu opioid receptor
649 defines shell and core of the ventral striatum. Neuroscience *75*, 777-792.
650 Waelti, P., Dickinson, A., and Schultz, W. (2001). Dopamine responses comply with basic
651 assumptions of formal learning theory. Nature *412*, 43-48.
652 Wolf, F.A., Angerer, P., and Theis, F.J. (2018). SCANPY: large-scale single-cell gene
653 expression data analysis. Genome Biol *19*, 15.
654 Xie, Z., Adamowicz, W.O., Eldred, W.D., Jakowski, A.B., Kleiman, R.J., Morton, D.G.,
655 Stephenson, D.T., Strick, C.A., Williams, R.D., and Menniti, F.S. (2006). Cellular and
656 subcellular localization of PDE10A, a striatum-enriched phosphodiesterase. Neuroscience *139*,
657 597-607.
658 Young, M.D., and Behjati, S. (2020). SoupX removes ambient RNA contamination from droplet
659 based single-cell RNA sequencing data. bioRxiv, 303727.
660 Zeisel, A., Hochgerner, H., Lönnerberg, P., Johnsson, A., Memic, F., van der Zwan, J., Häring,
661 M., Braun, E., Borm, L.E., La Manno, G.*, et al.* (2018). Molecular Architecture of the Mouse
662 Nervous System. Cell *174*, 999-1014.e1022.

663 Zhang, Y., Chen, K., Sloan, S.A., Bennett, M.L., Scholze, A.R., O'Keeffe, S., Phatnani, H.P.,
664 Guarnieri, P., Caneda, C., Ruderisch, N.*, et al.* (2014). An RNA-sequencing transcriptome and
665 splicing database of glia, neurons, and vascular cells of the cerebral cortex. J Neurosci *34*,
666 11929-11947.
667 Zhu, Y., Li, M., Sousa, A.M.M., and Šestan, N. (2014). XSAnno: a framework for building
668 ortholog models in cross-species transcriptome comparisons. BMC Genomics *15*, 343.
669 Zhu, Y., Sousa, A.M.M., Gao, T., Skarica, M., Li, M., Santpere, G., Esteller-Cucala, P., Juan, D.,
670 Ferrández-Peral, L., Gulden, F.O.*, et al.* (2018). Spatiotemporal transcriptomic divergence across
671 human and macaque brain development. Science *362*, eaat8077.

672

673

Figure S1

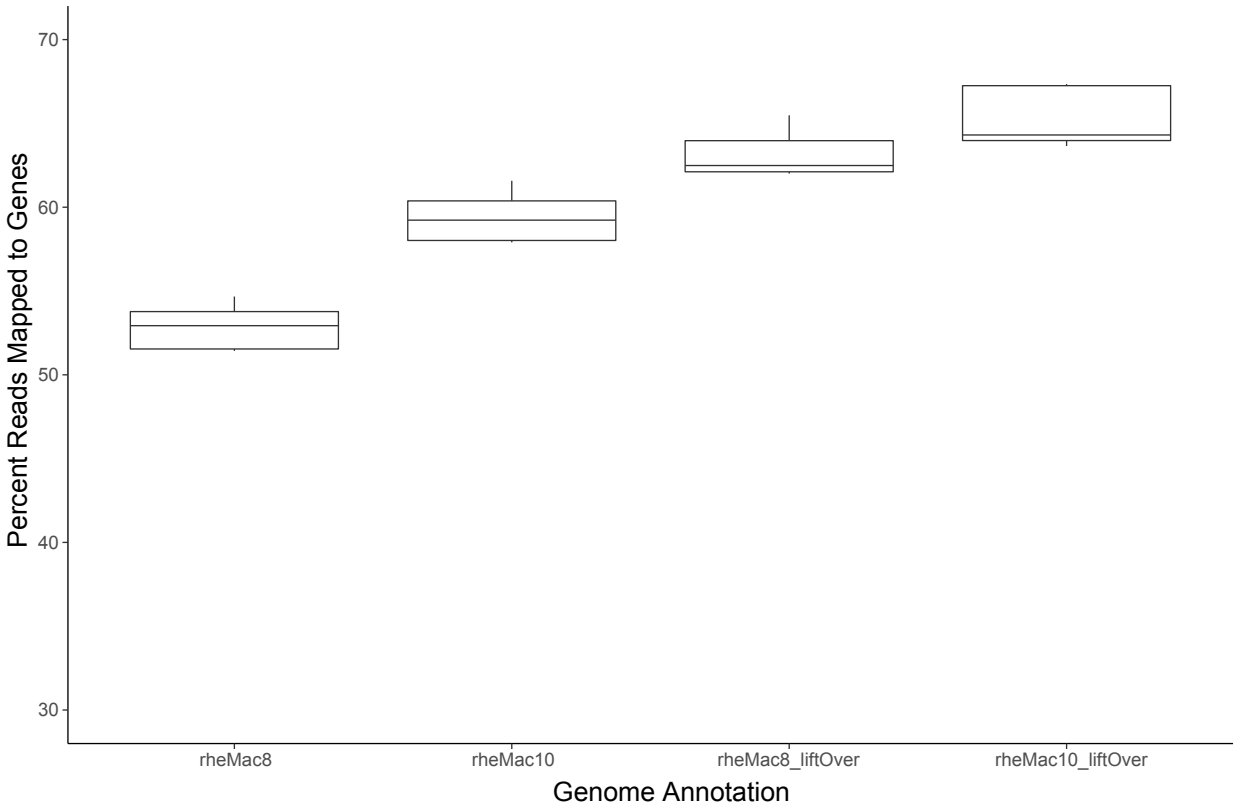
Percent Reads Mapped to Genes
70
60
50
40
30
rheMac8
rheMac10
rheMac8_liftOver
rheMac10_liftOver
Genome Annotation

Figure S2

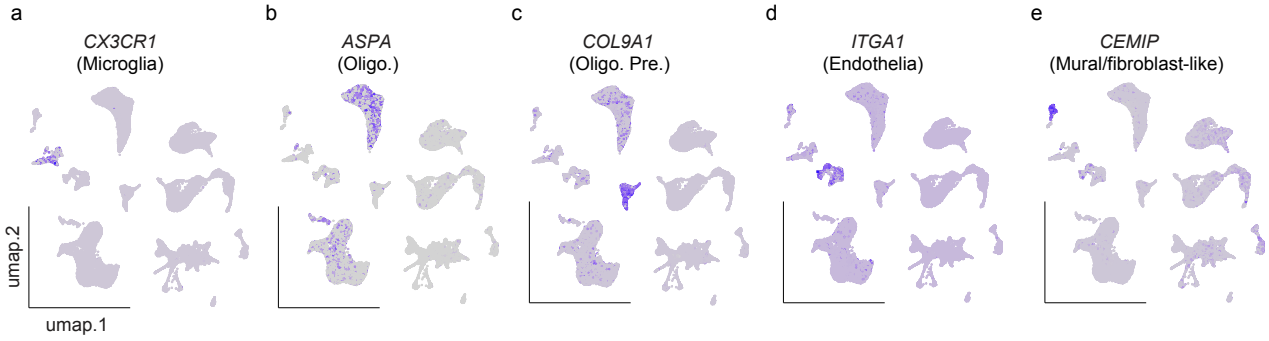
a
CX3CR1
(Microglia)
b
ASPA
(Oligo.)
c
COL9A1
(Oligo. Pre.)
d
ITGA1
(Endothelia)
e
CEMIP
(Mural/fibroblast-like)
umap.2
umap.1

Figure S3

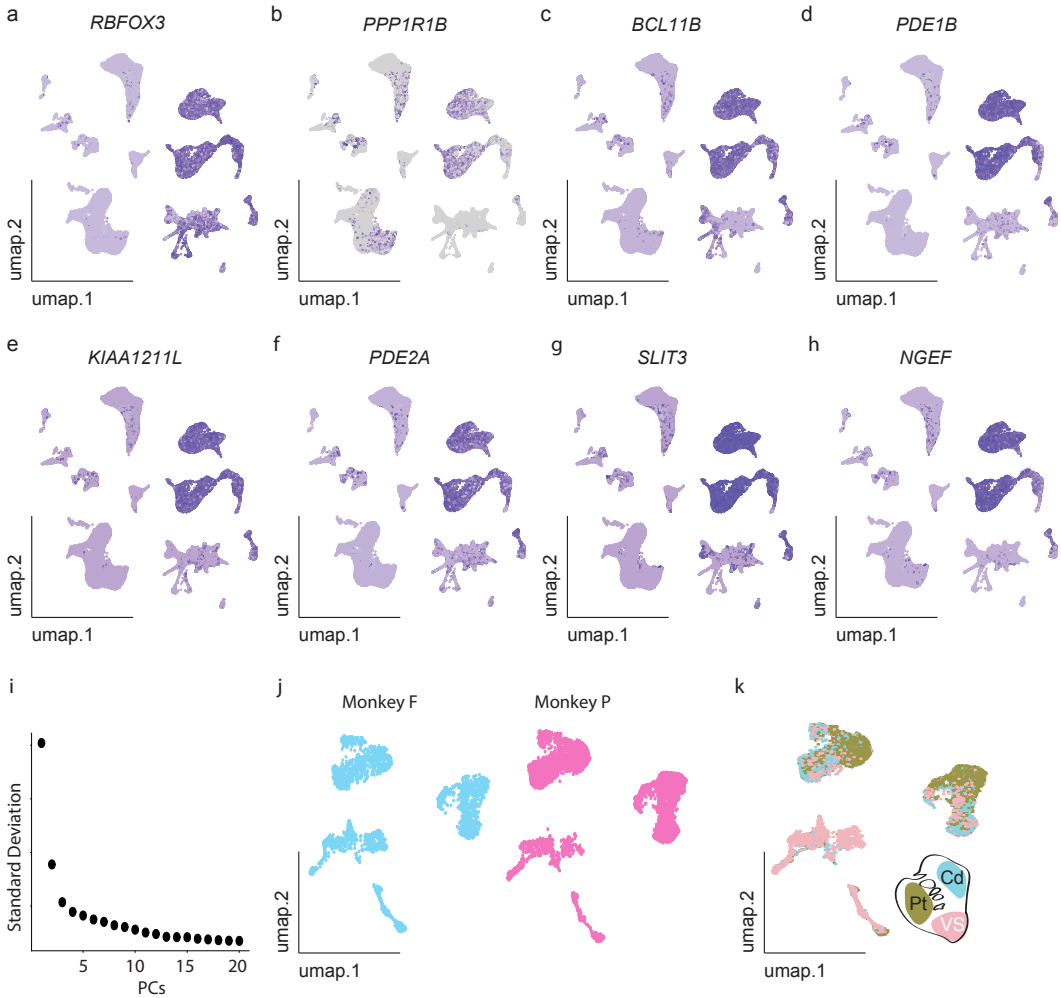
a
RBFOX3
b
PPP1R1B
c
BCL11B
d
PDE1B
e
KIAA1211L
f
PDE2A
g
SLIT3
h
NGEF
umap.2
umap.1
i
Standard Deviation
5
10
15
20
PCs
j
Monkey F
Monkey P
k
Cd
Pt
VS

Figure S4

a

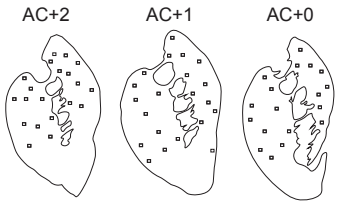

b

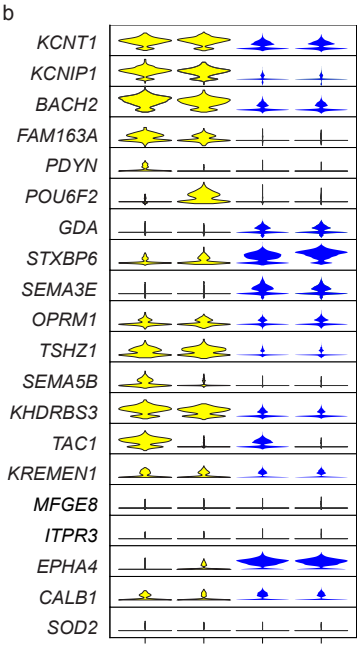

c

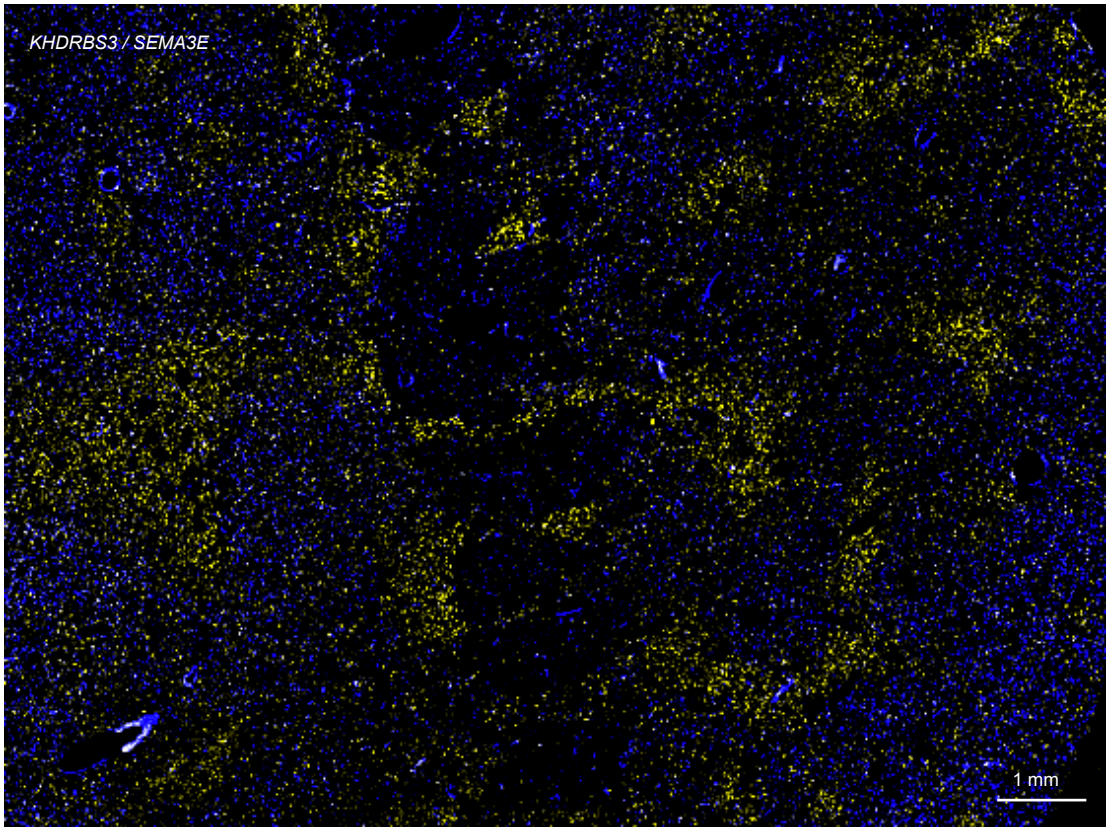

Figure S5

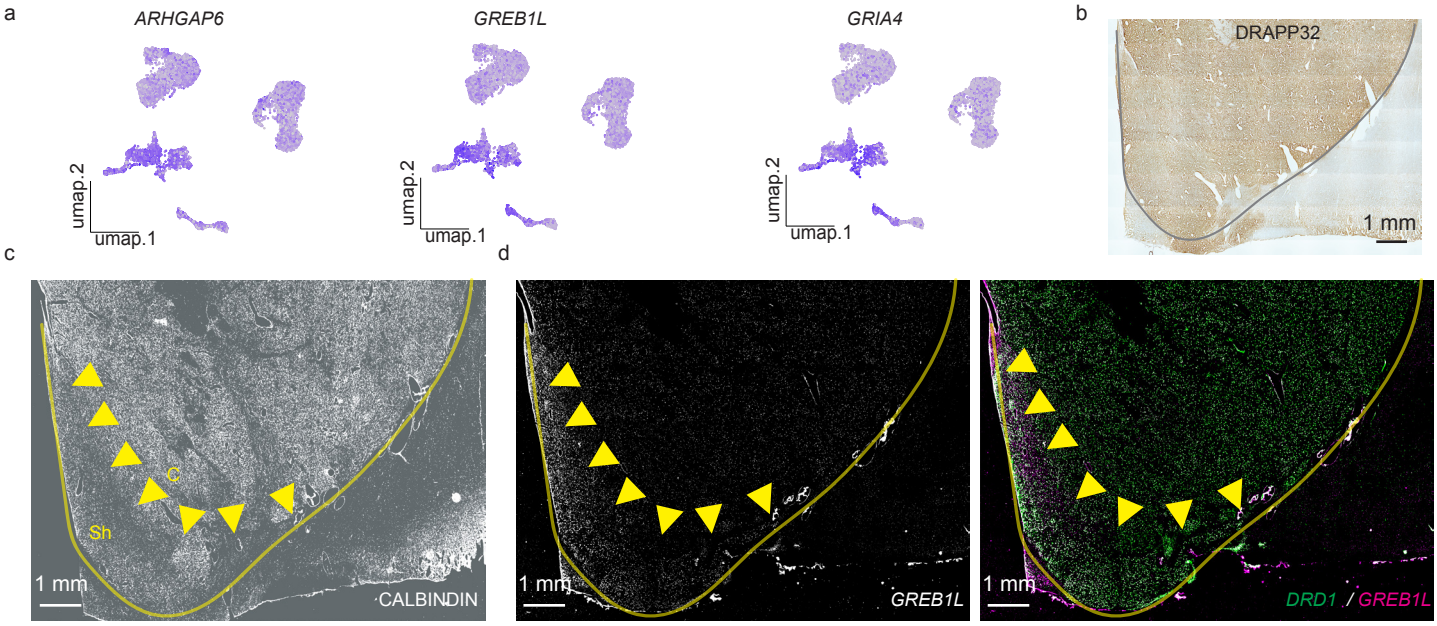
a
ARHGAP6
GREB1L
GRIA4
umap.2
umap.1
b
DRAPP32
1 mm
c
d
C
Sh
1 mm
CALBINDIN
GREB1L
DRD1 / GREB1L

Figure S6

a

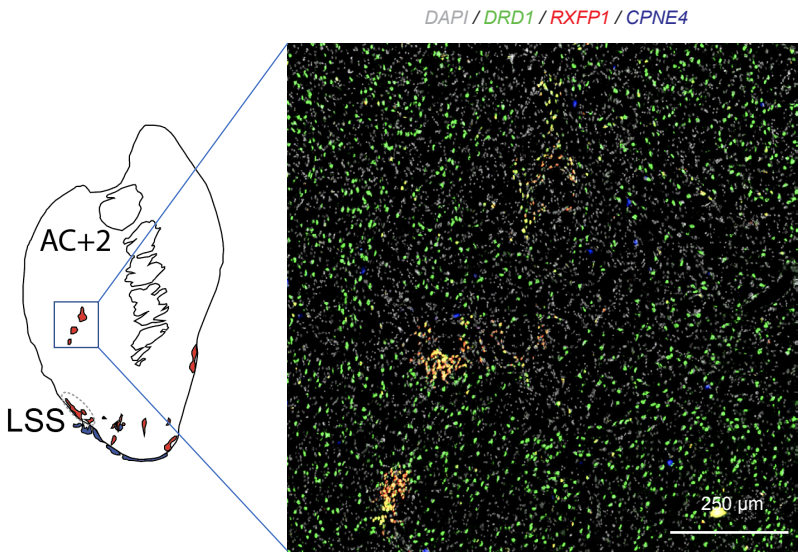

b

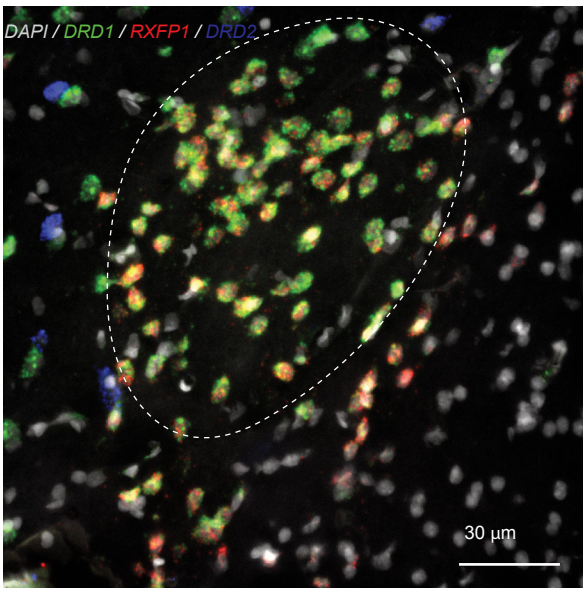
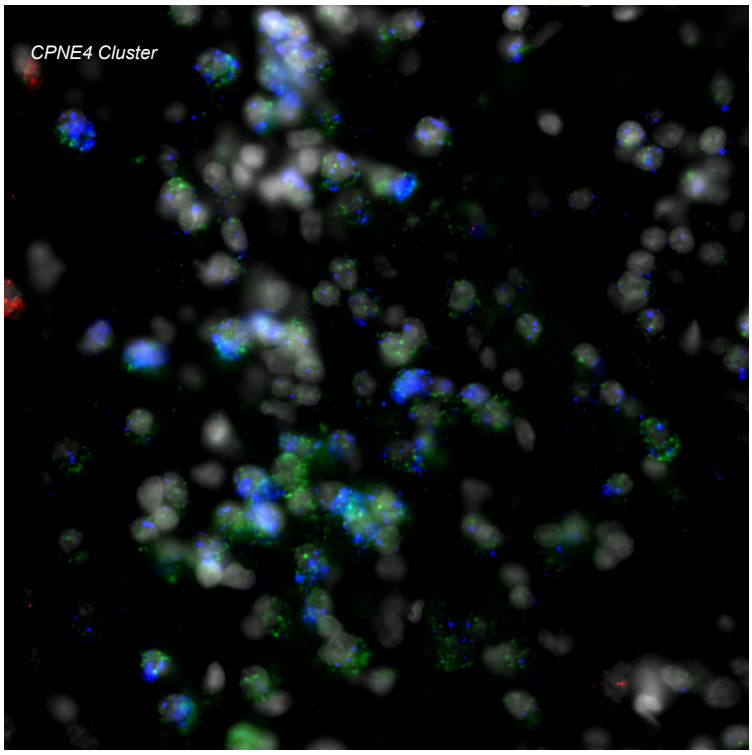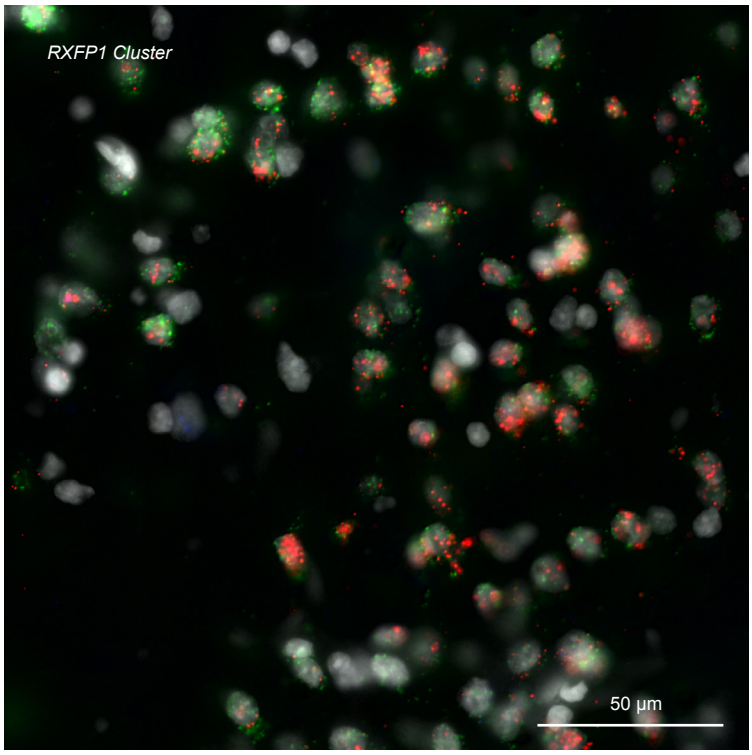
c